

Galaxy kinematics in the XMM2235 cluster field at $z \sim 1.4$ [★]

J. M. Pérez¹, B. Ziegler¹, M. Verdugo¹, A. Böhm² and M. Tanaka³

¹ Institute of Astrophysics (IfA), University of Vienna, Türkenschanzstr. 17, A-1180 Vienna, Austria.
e-mail: jm.perez@univie.ac.at

² Institute for Astro- and Particle Physics, University of Innsbruck, Technikerstr. 25/8, 6020 Innsbruck, Austria.

³ National Astronomical Observatory of Japan 2-21-1 Osawa, Mitaka, Tokyo 181-8588, Japan.

ABSTRACT

Aims. The relationship between baryonic and dark components in galaxies varies with the environment and cosmic time. Galaxy scaling relations describe strong trends between important physical properties. A very important quantitative tool in case of spiral galaxies is the Tully–Fisher relation (TFR) that combines the luminosity of the stellar population with the characteristic rotational velocity (V_{max}) taken as proxy for the total mass. In order to constrain galaxy evolution in clusters, we need measurements of the kinematic status of cluster galaxies at the starting point of the hierarchical assembly of clusters and the epoch when cosmic star formation peaks.

Methods. We took spatially resolved slit FORS2 spectra of 19 cluster galaxies at $z \sim 1.4$, and 8 additional field galaxies at $1 < z < 1.2$ using the ESO Very Large Telescope. The targets were selected from previous spectroscopic and photometric campaigns as [OII] and H_α emitters. Our spectroscopy was complemented with HST/ACS imaging in the F775W and F850LP filters mandatory for deriving the galaxy structural parameters accurately. We analyzed the ionized gas kinematics by extracting rotation curves from the two-dimensional spectra. Taking into account all geometrical, observational, and instrumental effects, these rotation curves were used to derive the intrinsic maximum rotation velocity.

Results. V_{max} was robustly determined for 6 cluster galaxies and 3 field galaxies. Galaxies with sky contamination or insufficient spatial rotation curve extent were not included in our analysis. We compared our sample to the local B-band TFR and the local Velocity-Size relation (VSR) finding that cluster galaxies are on average 1.7 magnitudes brighter and a factor 2 smaller. Cluster galaxies can be divided into two subsamples by the locii they occupy in the Tully-Fisher diagram, with half of the members each. For the high-mass sample the average deviation from the local TFR is $\langle \Delta M_B \rangle = -0.7$. This mild evolution may be driven by younger stellar populations (SP) of distant galaxies with respect to their local counterparts, and thus, an increasing luminosity is expected towards higher redshifts. However, the low-mass group consist of 3 highly overluminous galaxies with $\langle \Delta M_B \rangle = -2.5$ mag. This deviation can no longer be explained by the gradual evolution of SP with lookback time and thus, we suspect that we see rather compact galaxies that got an enhancement of star formation during their infall towards the dense regions of the cluster due to interactions with the intracluster medium.

1. Introduction

In the past years, we have got a good understanding of galaxy evolution from both observations and simulations. To mention a few examples, it is well established now that cosmic star formation (SF) rises strongly out to redshift 1 (Lilly et al. 1996) turning then into a plateau (Bouwens et al. 2007). At similar epochs quasar (AGN) activity of L_* -galaxies peaks (Hasinger et al. 2005). Deep fields reveal that $z = 1$ galaxies can already have obtained both regular elliptical and spiral morphologies. Hubble volume simulations are able to reproduce these basic facts (Angulo & White 2010). On the other hand, difficulties persist on some aspects like the mass-dependent shutting-down of SF by feedback processes (Bower et al. 2012) and the gas infall rate sustaining too high SF rates (Tonini et al. 2011). While it is possible to empirically model certain aspects (Peng et al. 2010), we still lack knowledge of the underlying physical mechanisms. For example, the relative contributions to galaxy mass growth by major mergers and gas accretion (Dekel et al. 2009) is still controversial.

A very important quantitative tool in case of spiral galaxies is the Tully–Fisher relation (TFR) that combines the luminosity of the stellar population (SP) with the characteristic rotational velocity taken as proxy for the total mass (including dark matter). It is well established in the local Universe (Pierce & Tully 1992) and was examined for evolution in recent years out to redshift 1 including work by our own group (Ziegler et al. 2003, Böhm et al. 2004, Böhm & Ziegler 2007 and Böhm & Ziegler 2016).

The traditional TFR is a subset of a more fundamental relation between baryonic mass (stellar and gas content) and rotational velocity. However, the gas mass fraction can only be observed directly for $z \sim 0$ galaxies. For nearby massive L_* -galaxies only a mild brightening was detected that translates into little overall evolution in the baryonic TFR (McGaugh et al. 2000). At higher redshift Puech et al. (2010) constructed this relation converting multi-color photometry into stellar masses assuming some SP model and estimating the gas mass fraction, finding no evolution up to $z \sim 0.6$. This indicates that a significant fraction of spirals have well established disks at $z=1$ and don't undergo major mergers until $z = 0$. Dutton et al. (2011) further show that the observed evolution of the scaling relations involving circular velocity, mass and size are consistent with a simple CDM-based model of discs growing inside evolving

[★] Based on observations with the European Southern Observatory Very Large Telescope (ESO-VLT), observing run ID 091.B-0778(B).

NFW dark matter haloes. However, challenging measurements of 2-dim. velocity fields at $z \approx 0.5$ reveal disturbances that can be explained by ongoing mass growth via accretion or minor mergers (Puech et al. 2008, Kutdemir et al. 2008, Kutdemir et al. 2010).

In contrast, massive SF galaxies at earlier epochs around $z \geq 2$ can display various kinematic behaviours from disk rotation via dispersion dominance to major mergers (e.g. Genzel et al. 2006, Förster Schreiber et al. 2009, Lehnert et al. 2009). It was recently found by Wisnioski et al. (2015) using data from the *KMOS*^{3D} survey that 93% of galaxies at $z \sim 1$ and 74% at $z \sim 2$ are rotationally supported, as determined from a continuous velocity gradient and $v_{rot}/\sigma_0 > 1$ while they showed a disk fraction of 58% when applying the additional stricter criteria that the projected velocity dispersion distribution peaks on or near the kinematic center, the velocity gradient is measured along the photometric major axis (for inclined systems), and the kinematic centroid is close to the center of the galaxy continuum. In contrast, applying the morpho-kinematic classification to a *KMOS*^{3D} subsample Rodrigues et al. (2016) found that only 25% of $z \sim 1$ galaxies are virialized spirals according to their morpho-kinematic classification. Simons et al. (2016) studied 49 galaxies from CANDELS fields with the Keck/MOSFIRE spectrograph finding that high mass galaxies ($\log M/M_\odot > 10.2$) at $z \sim 2$ are generally rotationally supported, fall on the TF relation, and have formed primitive disks with high gas velocity dispersion, while in contrast, a large fraction of less massive galaxies at this epoch are in the early phases of assembling their disks.

A sample of 14 galaxies at $z \sim 2$ galaxies was studied by Cresci et al. (2009) who found a significant offset in the M_* -TFR with increased scatter compared to local samples, which is even more prominent in the $z = 3$ study of Gnerucci et al. (2011). This implies a strong evolution within 2–3 Gyr with massive SF galaxies changing dramatically their dynamical state before settling into a more quiescent epoch at $z=1$. This demands thorough measurements of spatially resolved emission lines of galaxies at $z=1-2$ in order to understand this transition and its possible causes. A first study by Miller et al. (2012) exploited ultradeep Keck spectroscopy of the most suitable targets in five deep fields (EGS, SSA22, GOODS N&S, COSMOS) that benefit from multi-wavelength coverage. They find that most galaxies follow a M_* -TFR with a mild offset but strongly increased scatter compared to the local TFR. In a similar way Vergani et al. (2012) found a lack of any large evolution of the fundamental relations of star-forming galaxies in at least the past 8 Gyr using a sample of 46 galaxies at $1 < z < 1.6$ from MASSIV (Mass Assembly Survey with SINFONI in VVDS). In contrast, Tiley et al. (2016) found an offset of the Tully-Fisher relation for rotationally supported galaxies at $z \sim 1$ to lower stellar mass values (-0.41 dex) for a given dynamical mass but no significant offset in the absolute K-band TFR over the same period, contrary to some previous studies conducted at similar redshift but in broad agreement with the predictions of hydrodynamical simulations of EAGLE.

Most of these studies were restricted to the field population while in clusters additional specific effects should affect the content and structure of galaxies. Galaxy clusters provide special environments to test galaxy evolution across different cosmic epochs. Compared to the field, the number density of galaxies is high, and the relative velocities are large. The gravitational potential of a cluster is filled by the intracluster medium (ICM), a hot X-ray-emitting gas, and the overall mass-to-light ratio is much larger than for the individual galaxies, indicating the presence of vast amounts of dark matter. This environment exerts a

strong influence on the evolution of the cluster galaxies superposed on the (field) evolution that arises from the hierarchical growth of objects and the declining star formation rates over cosmic epochs. Besides tidal interactions between galaxies, including merging, as can also be observed in the field, cluster members are affected by cluster-specific phenomena related to the ICM (like ram pressure stripping) or the structure of the cluster (like harassment). Imprints of these interactions can be seen not only in present-day clusters, but they also manifest themselves in a strong evolution of the population of cluster galaxies. One example is the photometric Butcher-Oemler effect of an increasing fraction of blue galaxies with redshift (Butcher & Oemler 1978) implying a rising percentage of star-forming galaxies.

However, comparisons between the TFRs of cluster and field galaxies show no clear results. Milvang-Jensen et al. (2003) and Bamford et al. (2005) found higher B-band luminosities in clusters compared to the field, while Moran et al. (2007) presented a larger scatter for cluster galaxies. On the other hand cluster and field populations follow the same trends with no significant differences between these two environments according to Ziegler et al. (2003), Nakamura et al. (2006), Jaffé et al. (2011), Mocz et al. (2012) and Bösch et al. (2013). These discrepancies may stem from the necessity to utilize only regular rotation curves (RC) for a proper TF analysis that is based on the virial theorem.

In order to extend such measurements to higher redshifts and to investigate possible biases, we here present a kinematic study of the massive cluster XMMUJ2235-2557 (Mullis et al. 2005) at $z \sim 1.4$. This epoch marks the starting point of the hierarchical assembly of clusters and the build-up of the color-density relation. Making use of the multiwavelength data including HST imaging (Rosati et al. 2009, Strazzullo et al. 2010) that allows determination of morphologies and accurate derivation of structural parameters (needed for a proper kinematic analysis), we scrutinize the environmental dependence of disk galaxy scaling relations at the highest redshift to date.

The structure of this paper is as follows: In § 2, we describe the target selection, observation conditions and spectroscopic data reduction. The description of the photometric properties of our sample and details on the derivation of the structural parameters and maximum rotation velocities are shown in § 3. We present and discuss our results in § 4, followed by a short summary in § 5. Throughout this article we assume a Chabrier (2003) initial mass function (IMF) and adopt a flat cosmology with $\Omega_b=0.7$, $\Omega_m=0.3$, and $H_0=70 \text{ km s}^{-1} \text{ Mpc}^{-1}$. Magnitudes quoted in this paper are in the AB system.

2. Sample selection and observations

We carried out multi-object spectroscopy (MXU) with FORS2 between September 2013 and July 2014 to obtain the spectra of 27 galaxies with one mask. We chose the holographic grism 600z+23 that covers $\sim 3300\text{\AA}$ in the wavelength range 7370 – 10700 \AA . The slits were tilted and aligned to the apparent major axis of the targets in order to minimize geometrical distortions. Slit tilt angles θ were limited to $|\theta| < 45^\circ$ to ensure a robust sky subtraction and wavelength calibration. We used a slit width of 0.7" that delivers an instrumental resolution of $\sigma_{ins} = 65 \text{ km/s}$. This configuration yielded a spectral resolution of $R \sim 1400$ and an average dispersion of 0.81 $\text{\AA}/\text{pix}$ with an image scale of 0.25"/pixel. The total integration time for the MXU observations was 9h per target. In order to diminish the number of cosmic ray hits in our spectra, the observations were divided into 12 Observing Blocks (OBs) of one hour each with three sub-

exposures of 15 min per OB plus overheads. We achieved seeing conditions of 0.73 arcsec FWHM on average.

The primary targets for the kinematic analysis were 15 cluster galaxies with measured spectroscopic redshifts and [OII] λ 3727 Å emission. These galaxies were extracted from catalogues of previous spectroscopic campaigns in the same cluster field (V. Strazzulo & M. Tanaka, *priv. comm.*). Another set of 5 galaxies with photometric redshift from deep narrow-band imaging corresponding to the rest-frame wavelength of $H\alpha$ were selected from Grützbauch et al. (2012) at the cluster's redshift. The remaining available mask space was filled with galaxies of disk-like appearance and appropriate position angle, but unknown redshift, yielding in total 27 targets.

We performed the spectroscopic data reduction mainly using the ESO-REFLEX pipeline for FORS2 (version 1.19.4). The main reduction steps were bias subtraction, flat normalization and wavelength calibration. The last one was improved by removing some lines from the catalogue of arc lines. Additionally we performed bad pixel and cosmic ray cleaning co-adding the exposures with a sigma-clipping algorithm using IRAF. We show the coordinates, redshifts, rest frame colors and magnitudes of our final sample in Table 2.

3. Methods

3.1. Imaging and Photometry

To complement the spectroscopy, we made use of imaging data from a variety of sources, including HST/ACS (F775W & F850LP), VLT/FORS2 (B, R, z-bands), VLT/VIMOS (U-band), VLT/HAWKI (J & Ks-bands), CTIO/ISPI (H-band) and Spitzer IRAC (3.6 μ m & 4.5 μ m), encompassing thus from the rest-frame UV to NIR at the cluster redshift. The characteristics of these datasets are described in Table 1.

The HAWKI data reduction is described in Lidman et al. (2008) and the processed images were subsequently released as Phase 3 products in the ESO archive, from where we retrieved them. Zeropoints were also provided in the Vega system which we transform to the AB system.

The FORS2 and VIMOS images were also retrieved from the ESO archive as raw data. Similarly the CTIO-Blanco/ISPI H-band raw frames were downloaded from the NOAO science archive. These datasets were processed with the THELI pipeline (Schirmer 2013), which takes care of all basic reduction steps as well as the astrometric calibration and co-addition. Photometric calibration for the FORS2 B & R and the VIMOS U-band images was performed using a two step approach. Firstly zeropoints were fixed to the official ones available at the ESO webpages. However noticeable differences were detected in the color of stars in comparison to stellar libraries (Pickles 1998). We therefore produced synthetic colors for all available bands and compared them to the observed ones using the stellar locus method (e.g. Kelly et al. 2014), adjusting them until all differences were minimal. The applied corrections ranged from 0.3 to 0.6 magnitudes.

There was no zeropoint available for the FORS2 z-band. Fortunately the filter transmission curve is nearly identical to the HST/ACS F850LP filter available for a significant part of the field. Therefore the FORS2 z-band was calibrated against that latter dataset. The ISPI H-band was calibrated using 2MASS stars available in the field and transformed to the AB system. The remaining space based images were retrieved fully processed and calibrated so no additional steps were necessary before performing the photometry.

The spatial coverage of the different datasets can be seen in Fig. 1, where we also mark the targets of the spectroscopic campaign. As it can be seen not all galaxies have measurements in all bands. However, they do have enough measurements across a large wavelength range to reliably determine all parameters necessary for our analysis.

Because of the varying depth, field of view, point spread function, pixel scales and quality of the imaging, special care must be taken in performing the photometry for our target galaxies. We therefore deviate slightly from the standard approaches that use more homogeneous datasets. In particular we chose to not degrade the high quality imaging (HST and HAWKI) to the worst seeing. We neither rebinned the images to match the pixel sizes of the rest of the imaging as required by dual band photometry. Instead we chose to measure magnitudes within an elliptical Kron aperture (Kron 1980) matched to the seeing in each image. To calculate the size of the Kron aperture we use SExtractor (Bertin & Arnouts 1996) in the high quality data where we measure the coordinates, the Kron radius, the ellipticity, the position angle and the Kron magnitudes (MAG_AUTO). These parameters were passed to the python PHOT_UTILS tools, which replicate many of the functionalities found in SExtractor in a more flexible environment.

To calculate how much the Kron apertures need to grow to take into account the different seeing values in the other bands, we use the software STUFF and SKYMAKER (Bertin 2009) to simulate realistic galaxy fields with different spatial resolutions, where we ran SExtractor with the same parameters over the same galaxies. In general the Kron radii growth can be modeled as a simple linear function that depends only on the measurements in the high quality imaging and the seeing in the lower quality imaging. Magnitudes computed by PHOT_UTILS using the derived apertures are in excellent agreement (at ~ 0.1 mag level) with those determined directly by SExtractor.

The above procedures were however not applied to the Spitzer images. With a PSF FWHM of ~ 2 arcsec, distant galaxies are effectively unresolved in the IRAC images. We therefore use a fixed circular aperture of 6 arcsec and apply the standard correction factors for the missing flux (factors 1.205 & 1.221 in the 3.6 and 4.5 μ m bands respectively).

3.2. Stellar masses and rest-frame magnitudes

Rest frame magnitudes and stellar masses were determined using the code LEPHARE of Arnouts & Ilbert (2011) (see also Ilbert et al. 2006) which fits stellar population synthesis models (Bruzual & Charlot 2003) to the spectral energy distribution (SED) derived from the photometry. The code is a simple χ^2 minimization algorithm that finds the best match of templates for the given data. To avoid overfitting we restrict the possible ages to values smaller than the age of the Universe at the redshift of the cluster.

To put in context our sample of cluster galaxies, we present in Fig. 2 the color-magnitude diagram in J and K-bands for XMMJ2235 galaxy members. The cluster red sequence fit from Lidman et al. (2008) is shown with a black line, with red sequence galaxies defined as galaxies redder than 0.2 magnitudes blueward of this fit. The purpose of this comparison is to highlight the nature of our cluster galaxies with [OII]-based kinematics. We would like to mention that two of our galaxies (IDs 8 and 11 in Table 2) were part of the Herschel sample of dust-obscured star-forming galaxies presented in Santos et al. (2013).

Edge-on disks have higher extinction (A_B) than face-on ones and more massive disks are dustier than less massive ones Giovanelli et al. (1995). We corrected the rest frame B-band absolute

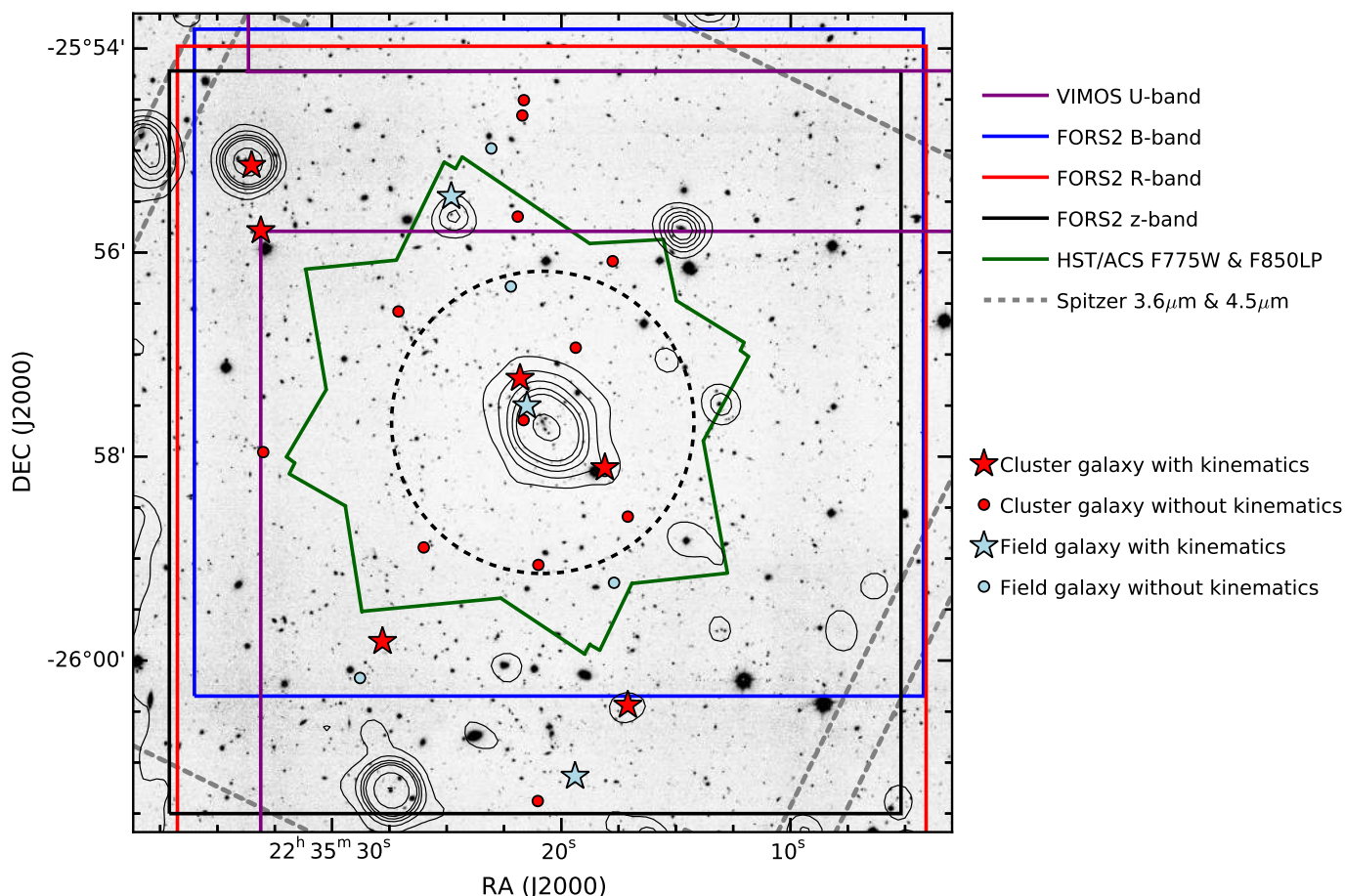


Fig. 1. A portion (8.25×8.25 arcmin²) of the J-band HAWKI image with XMM-Newton X-ray contours overlaid. The field of view of the different instruments used in this work is also shown. The HAWKI J & Ks and ISPI H-band observations cover a field of view much larger than the figure. The FORS2 B-, R- and z-band coverage was obtained from different ESO programs. Most of the X-ray sources are likely distant AGNs, however the extended emission associated to the cluster can be appreciated in the center. The dashed circle marks the $R_{500} = 0.75$ Mpc radius derived by Rosati et al. (2009). We denote the position of the galaxies analyzed in this study distinguishing between field and cluster and between those which yielded a V_{max} value and those which did not.

Table 1. Summary of the imaging data used in this work

Telescope	Instrument	Filter	Exp. Time (s)	PSF FWHM (")	PID
VLT	VIMOS	U	21 600	0.80	079.A-0758
...	FORS2	B	1 590	0.72	087.A-0859
...	...	R	2 250	0.75	072.A-0706, 073.A-0737
...	...	z	1 200	0.40	274.A-5024, 091.B-0778
...	HAWKI	J	10 560	0.47	060.A-9284(H)
...	...	Ks	10 740	0.32	...
CTIO/Blanco	ISPI	H	1 200	1.07	2009B-0484
HST	ACS/WFC	F775W	13 500	0.10	10496, 10531, 10698
...	...	F850LP	14 400	0.10	...
Spitzer	IRAC	3.6 μ m	6 262	1.95	20760
...	...	4.5 μ m	6 262	2.02	...

magnitudes for intrinsic dust absorption following the approach by Tully et al. (1998):

$$A_B = \log(a/b)[-4.48 + 2.75 \log(V_{max})] \quad (1)$$

The extinction is dependent on the inclination angle i , which is related to the ratio between the axes (a/b), and on the V_{max} of

every galaxy. After applying the extinction correction the typical errors in B-band luminosity range from 0.1 to 0.2 dex.

3.3. Structural Parameters

Due to the relatively small spatial coverage of the HST images in this cluster, we were able to derive the structural parameters of galaxies from the z-band (F850LP) images only in the central

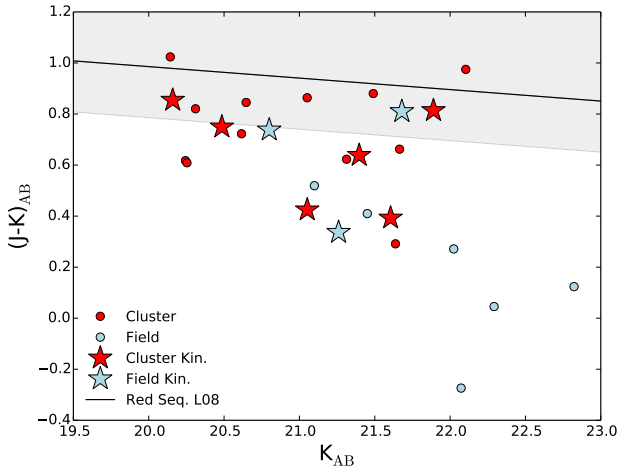


Fig. 2. Color Magnitude diagram. Red stars and circles define spectroscopic cluster members with and without derived kinematics in our sample respectively. Blue stars and circles show field galaxies with and without derived kinematics in our sample respectively. The cluster red sequence fit derived by Lidman et al. (2008) is shown as a black line with a shaded area: red sequence galaxies are defined as galaxies redder than 0.2 magnitudes blueward of this fit, which is shown with a shaded area. Magnitudes and colors are given in the AB system.

regions of the cluster. For galaxies far from the cluster center we used ground based HAWKI photometry in K-band. We used the GALFIT package by Peng et al. (2002) that allows to fit multiple two dimensional surface brightness profiles simultaneously to the galaxy under scrutiny. We fitted the surface brightness profiles of the galaxies of our sample using two different methods:

1. A single Sérsic profile with free index n_s .
2. A two-component model with an exponential profile for the disk and a de Vaucouleurs profile ($n_s = 4$) for the bulge.

The best parameters from the first method were used as initial guess values for the second. All fit residuals were visually inspected (Fig. 6) and in a few cases, it was necessary to apply constraints on some parameters in order to avoid a local minimum in the fitting process. We used the bulge/disk decomposition to obtain the disk parameters when possible within the HST coverage. However, an accurate structural decomposition was not feasible with the ground-based K-band data due to the limited spatial resolution. We therefore restricted the GALFIT models to a single Sersic profile for galaxies without available HST imaging. We stress that for the analysis presented here, the most important parameters are the ratio between the axes (a/b), position angle θ , and scale length R_d of the disk.

However, observed scale lengths depend on the wavelength regime. It was shown in de Jong (1996) that R_d is smaller when galaxies are observed in redder filters. In effect, HAWKI K-band-based scale lengths are 15% smaller than z-band-based ones. We corrected these scale lengths to make them comparable by using the linear fit between the half-light radii (r_e) and the rest frame central wavelength for disk galaxies shown in Kelvin et al. (2012). GALFIT only returns random errors on the best-fit parameters. These are very small ($<1\%$) throughout our sample. We relied on a previous analysis of HST/ACS images using GALFIT in Böhm et al. (2013) to obtain a more realistic estimate of the systematic errors on R_d . In that work, a typical systematic error of 20% on galaxy sizes was found for a negligible central point source. This value hence represents the systematic size

error for galaxies with the light profiles of pure disks or disks with only weak bulges; this is the case for the vast majority of galaxies in our sample. We therefore adopt this error on R_d in the following.

The inclination i is the angle between the normal vector of the disk and the line-of-sight. We computed it from the apparent major axis a and the apparent minor axis b following Heidmann et al. (1972):

$$\cos^2(i) = \frac{(a/b)^2 - q^2}{1 - q^2} \quad (2)$$

Here the factor q is the ratio between disk scale length and scale height and it is fixed to 0.2, which is the observed value for typical spirals in Tully et al. (1998).

The position angle θ denotes the orientation of the apparent major axis in the plane of the sky. Throughout this paper the convention will be that θ gives the angle between the apparent major axis and the horizontal axis, counted counter-clockwise. To minimize the geometric distortions we constrain the mismatch angle δ that gives the deviations between the major axis and the slit direction of a certain galaxy to $\delta \leq 30^\circ$.

3.4. Rotation-curve extraction and modelling

Our approach to extract rotation curves from spatially resolved spectra and determine V_{max} is explained in detail in Böhm et al. (2004), Bösch et al. (2013), Böhm & Ziegler (2016). A summary of the main steps is presented here:

Prior to the emission line fitting we use an averaging boxcar of three pixels width, corresponding to $0.75''$, for each spatial position in the spectrum to enhance the signal-to-noise ratio (S/N). We then transform red- and blueshifts of the emission lines as a function of galactocentric radius into an observed position-velocity diagram. The kinematic centre is determined by minimizing the asymmetry of the observed RC, with a maximum allowed mismatch between kinematic and photometric center of ± 1 pixel, corresponding to ~ 2 kpc at the redshifts of our targets.

To determine V_{max} for a given galaxy, we simulate its rotation velocity field taking into account all geometric effects like disk inclination angle and observational effects like seeing or the influence of the slit width. The simulated velocity field is generated assuming a linear rise of the rotation velocity $V_{rot}(r)$ at $r < r_t$, where r_t is the turnover radius, and a convergence of $V_{rot}(r)$ into a constant value V_{max} at $r > r_t$ (Courteau 1997).

We set the turnover radius as equal to the scale length, R_d , measured from the stellar morphology (GALFIT). In the last step we extract from the synthetic velocity field a simulated rotation curve from which we obtain the intrinsic maximum rotation velocity V_{max} taking into account the structural and observational parameters. The typical error on V_{max} at a given galactocentric radius is 10-20 km/s. For a complete description of the full process we cite again Böhm et al. (2004). Three examples of the synthetic velocity fields, simulated and observed rotation curves of our sample are shown in Fig. 6.

Although we observed 27 objects, only 25 of them turned out to be emission line galaxies after the analysis of their spectra. Redshift values were computed using IRAF under visual determination of [OII] emission line center, that is the only emission line available for cluster members. We detected 17 cluster members and 8 field galaxies. However, part of the cluster sample was affected by strong sky line contamination. As a result, 8 cluster galaxies were discarded due to noisy contamination. We extracted 6 RCs of cluster members from the remaining 9

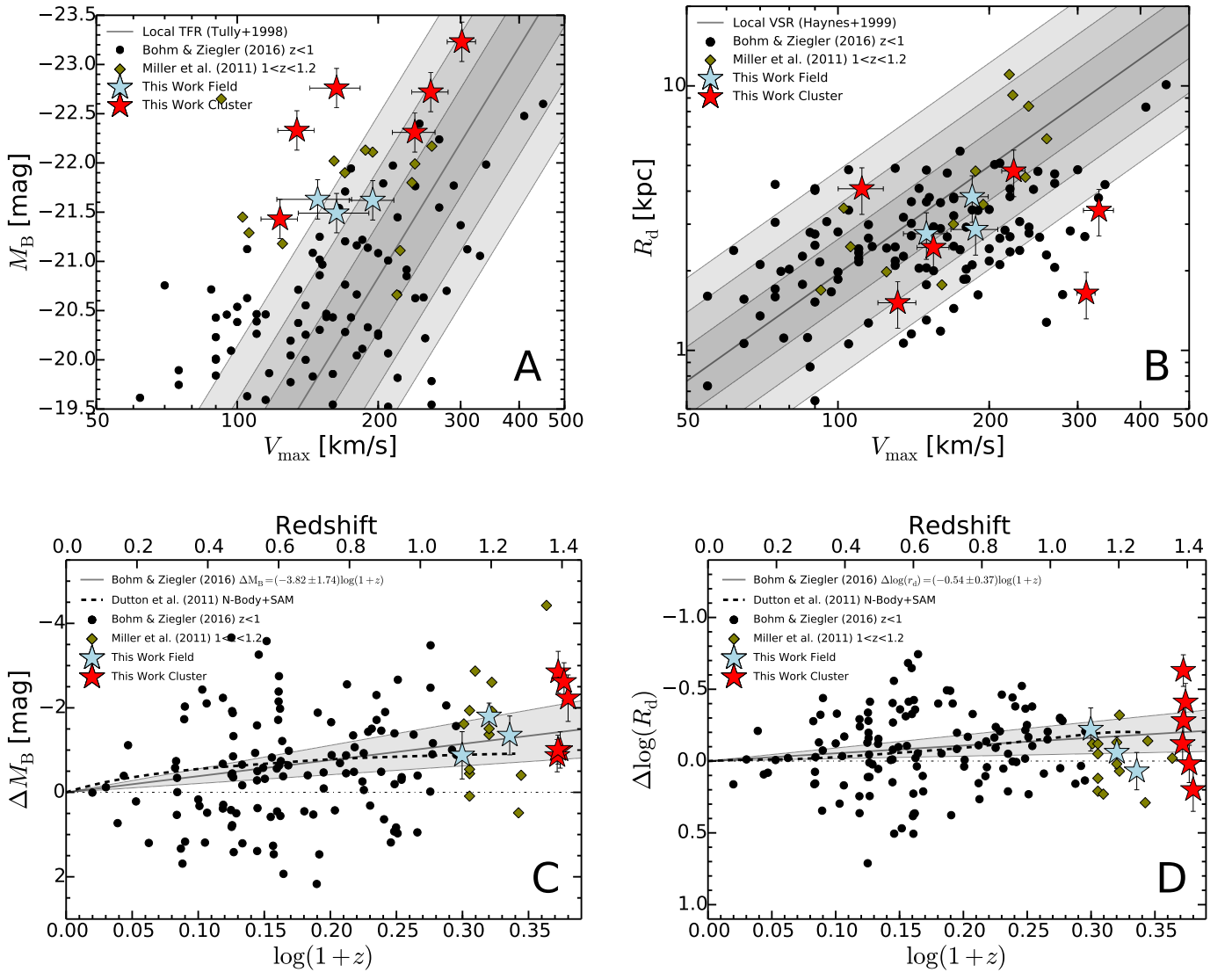


Fig. 3. A) Tully-Fisher B-band diagram. B) Velocity-Size relation. C) TFR evolution diagram. Offsets ΔM_B of galaxies in our sample from the local TF relation, displayed as a function of redshift. D) VSR evolution diagram. Offsets ΔR_d of galaxies in our sample with respect to the local VSR, displayed as a function of redshift. In A and B the grey line represents respectively the local TFR (Tully et al. 1998) and the local VSR (Haynes et al. 1999a) with 1σ , 2σ and 3σ shaded regions. Two sample of field galaxies were plotted for comparison: The first one comprises 124 disk galaxies out to $z=1$ from Böhm & Ziegler (2016) and is plotted with black circles. Miller et al. (2011) provided a second field sample composed by 13 disk galaxies at $1 < z < 1.3$ plotted as olive diamonds. The 3 field galaxies at $1 < z < 1.2$ targeted in our observations are plotted with blue stars. Cluster galaxies are represented by red stars.

galaxies, discarding 3 galaxies due to their very compact [OII] emission that prevents us from reaching the flat part in the RC. In addition 3 RCs were extracted from the field sample, discarding in the process 3 galaxies with sky contamination and two galaxies with compact emission.

4. Results and Discussion

The primary results of this paper are shown in Fig. 3 where we present the Tully-Fisher relation (TFR) and Velocity-Size relation (VSR) for cluster galaxies (red star symbols) at $z \sim 1.4$. In Fig. 3A we show the B-band TFR, that is related with recent episodes of star formation. The distribution of our kinematic sample is compared with the local TFR by Tully et al. (1998) and the local VSR derived by Böhm & Ziegler (2016) using data from Haynes et al. (1999b). In addition, two field samples within

$0.2 < z < 1.3$ are shown as comparison between different environments.

The first field sample comprises 124 disk galaxies out to $z=1$ from Böhm & Ziegler (2016) (hereafter BZ16) plotted as black circles. This is one of the largest kinematic samples of distant galaxies to date. A second field sample composed of 13 disk galaxies at $1 < z < 1.3$ selected by redshift from a bigger sample provided by Miller et al. (2011) (hereafter M11) is plotted as olive diamonds. We also display our 3 field galaxies targeted in our observations at $1 < z < 1.2$ (blue stars). On average, cluster galaxies in our sample are brighter by $\langle \Delta M_B \rangle = -1.7$ mag in B-band compared to the local TFR and smaller by a factor of 2 compared to the local VSR (figure 3 A and B respectively). In order to look for environmental effects we compare the results of our cluster sample with Miller’s field galaxies at similar redshift, finding that our cluster galaxies are brighter on average by

$\langle \Delta M_B \rangle = -0.3$ mag in B-band and smaller by a factor of 1.5 compared to their field counterparts. Considering the position of our cluster galaxies in the Tully-Fisher diagram (Fig. 3A), the cluster sample can be split into two groups: The first one is composed of three fast rotating ($V_{max} > 200$ km/s) and thus high total mass galaxies that are offset from the local TFR by roughly 2σ , $\langle \Delta M_B \rangle = -0.9$ on average. The second group is composed of 3 low-massive galaxies but offset by more than 5σ respect to the local TFR, $\langle \Delta M_B \rangle = -2.5$ on average. This indicates that different physical processes may be taking place in these subsamples due to the cluster environment. In addition, all cluster galaxies in our sample fall on the high-luminosity side of the local TF relation, but those cluster galaxies with V_{max} below 200 km/s are offset by more than 3σ respect to the local TFR, while this effect is much smaller for the rest of the sample.

Figure 3 C and D display the offsets ΔM_B and $\Delta \log R_d$ from the local TFR and VSR as a function of redshift. In panel C field galaxies show increasing over-luminosities towards higher redshifts despite the scatter of the samples. Extrapolating the linear fit given in Böhm & Ziegler (2016) (grey line) the luminosity evolution of field galaxies reaches $\Delta M_B = -1.2 \pm 0.4$ magnitudes at $z=1.4$. As explained before, our cluster sample is divided into two groups with one of them lying within the 1σ area of this fit, $\Delta M_B = -0.9 \pm 0.4$ magnitudes on average; while the other exhibits offsets that can not be explained by the expected luminosity evolution of field galaxies from previous observations nor numerical simulations (Dutton et al. 2011), $\Delta M_B = -2.5 \pm 0.5$ magnitudes on average. Field galaxies in our sample lie within the 1σ area of the predicted luminosity evolution, $\Delta M_B = -1.3 \pm 0.5$ magnitudes on average, and show good agreement with predictions from numerical simulations by Dutton et al. (2011) (dashed line) who found $\Delta M_B = -0.95$ mag. The errors on ΔM_B are computed through error propagation from the errors on V_{max} and M_B .

In panel D previous samples of field galaxies show decreasing sizes towards higher redshifts although the scatter of the samples is similar to the one found in C. According to the extrapolation of the linear fit given in BZ16 (grey line), the size evolution reaches $\Delta \log R_d = -(0.22 \pm 0.14)$ at $z=1.4$ where negative values in $\Delta \log R_d$ mean smaller sizes at a given maximum rotation velocity V_{max} . Our three field galaxies present $\langle \Delta \log R_d \rangle = (-0.12 \pm 0.07)$, falling within the 1σ area of the extrapolated evolution function for field galaxies at $z < 1$ presented in BZ16 and also consistent with M11. Predictions from numerical simulations by Dutton et al. (2011) (dashed line) showed that $\Delta \log R_d = -0.2$ at the same redshift. In this plot the $z=1.4$ cluster galaxies do not populate two separate groups but cover a broad range in size evolution. Nevertheless, on average they are consistent with the empirical findings and theoretical predictions, $\langle \Delta \log R_d \rangle = (-0.24 \pm 0.13)$. Errors on $\Delta \log R_d$ are computed through error propagation from the errors on V_{max} and R_d .

The brightening detected in the B-band TFR for cluster galaxies can be partially explained by the increasing star formation galaxies experience towards longer lookback times. However, the division of our sample into two groups according to their total mass and B-band luminosity offsets might indicate the presence of additional effects that may explain their properties. Several possible explanations have to be considered:

First, V_{max} might be underestimated. Persic et al. (1996) studied relation between the mass of a galaxy and the shape of its RC introducing a complex definition of universal rotation curve (URC). According to this study, very low-mass spirals show an increasing rotation velocity even at large radii, whereas the rotation curves of very high-mass spirals moderately decline in that regime. These gradients are found as far as 5 optical disk scale

lengths. However, our cluster sample mainly covers intermediate masses ($10.17 < \log M_* < 10.84$), where the URC does not introduce a velocity gradient at large galactocentric radii. Only one field galaxy with $\log M_* = 9.77$ may suffer from this effect. However, the spatial extent of the rotation curves in our sample (as well as other samples at similar redshifts) is around two to four times R_d , which is insufficient to constrain potential RC gradients in the outer disk. With our RCs, we probe out to radii similar to R_{opt} , and for galaxies with $V_{rot}(R = R_{opt}) > 100$ km/s (all of our galaxies), the largest possible underestimate if V_{max} due to RC gradients is 10–20% (see Fig. 4 in Persic et al. 1996).

We also checked whether these distributions are caused by a selection effect due to a magnitude limit in the spectroscopic and photometric campaigns from which we extracted our targets. Towards higher redshifts, such an apparent magnitude limit corresponds to higher luminosities and in turn higher masses. A fraction of the low-luminosity, low-mass (slowly rotating) spiral population is therefore missed in the selection process, while the low-mass galaxies that are selected might preferentially be located at the high-luminosity side of the TF relation. This effect is commonly known as Malmquist bias. Thus, in all redshifts bins, at a given V_{max} any distant galaxy sample with a magnitude limit will show an overluminosity of the low-mass galaxies compared to the local TFR, while the distributions are similar at the high-mass end. Some of the previous studies we used for target selection (Strazzullo et al. 2010, Grützbauch et al. 2012) have magnitude limits of $z_{AB} = 24$ and $H_{AB} = 24.4$. However, our sample is well inside the limits showing average observed magnitudes of $z_{AB} = 22.4$ and $H_{AB} = 21.3$, meaning that the magnitude bias in our target selection should not have a big impact. In addition we studied the distribution of our targets in B-band luminosity. The mean B-band luminosity value for the full sample is $\langle M_B \rangle = -21.7$ mag with a scatter of $\sigma_{total} = 0.9$ mag. As stated in section 2.4, 25 out of 27 galaxies showed [OII] emission but we didn't extract RC from all of them due to diverse causes (OH contamination, compactness, faintness). Neglecting galaxies whose emission lines are contaminated leaves us with a clean sample of 17 galaxies with the same $\langle M_B \rangle$ and scatter. This means that the removal of OH-affected galaxies does not introduce a luminosity bias to the clean sample. Now, if we focus on the cluster members we see that they have similar M_B but cover a large range in V_{max} . The high-mass (fast rotating) group shows higher M_B than the clean sample, $\langle M_B \rangle = -22.8$ with $\sigma_{high} = 0.6$, and high maximum rotation velocity, $\langle V_{max} \rangle = 289$ km/s. On the other hand, the overluminous low-mass (slowly rotating) group presents similar M_B but relatively low V_{max} , $\langle M_B \rangle = -22.2$ with $\sigma_{low} = 1.0$ and $\langle V_{max} \rangle = 133$ km/s. Thus, both groups have similar B-band luminosities but only the low-mass group is significantly offset respect to the local TFR, which might point towards the presence of a magnitude bias. Nevertheless the small number of galaxies make it hard to draw firm conclusions, and the large B-band offsets in the TFR ($\langle \Delta M_B \rangle = -2.5$ mag for the low-mass cluster galaxies) probably require additional, cluster-specific effects to explain the enhanced luminosities.

The third scenario suggests that we might see rather compact galaxies that got an enhancement of SF during their infall towards the dense regions of the cluster. If this is the case, this enhancement should be caused by a process that does not strongly affect galaxy gas kinematics, at least within the galactocentric radial regime probed by our RCs, up to ~ 3 scale lengths, and during the infall phase where the ICM density has low to intermediate values. Kronberger et al. (2008b) and Kapferer et al. (2009) investigated the influence of ram pressure stripping (RPS)

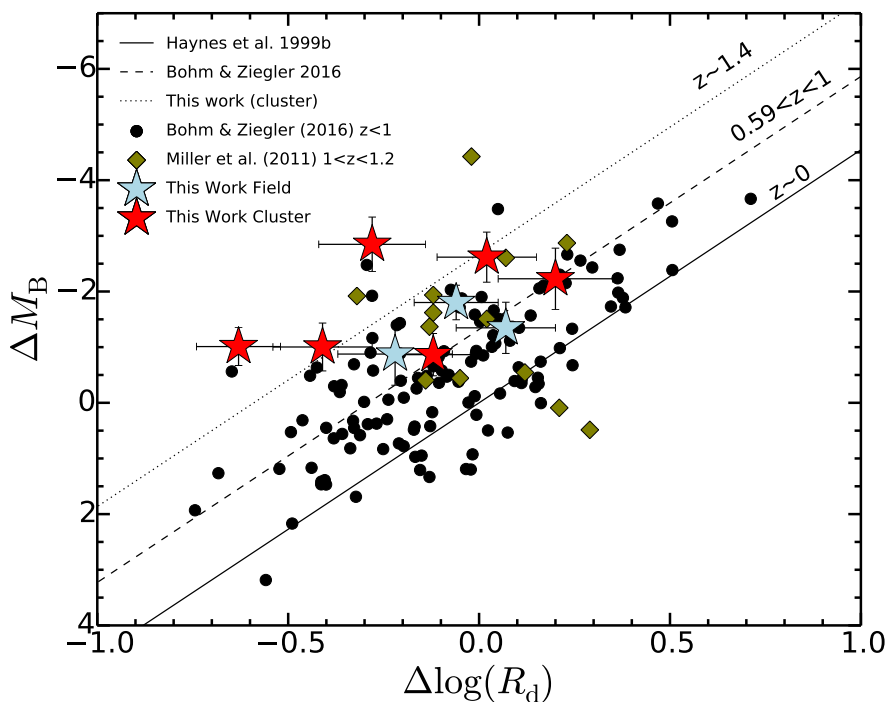


Fig. 4. Correlation diagram between the offsets, ΔM_B , from the TFR and the offsets, $\Delta \log R_d$, from the VSR for previously presented samples. The solid line shows the linear fit for galaxies studied in the local universe (Haynes et al. 1999b). By definition, this line goes through the coordinates origin. The dashed black lines plotted in this diagram show the linear fit for galaxies studied in Böhm & Ziegler (2016) at $0.59 < z < 1$, showing that galaxies are shifting away with lookback time towards higher luminosity and smaller sizes. The dotted black line is the linear fit at fixed slope for our cluster sample whose zero point is shifted by -0.6 dex in $\Delta \log R_d$ with respect to the local sample.

on the internal gas kinematics of simulated spiral galaxies focusing on how the resulting distortions of the gaseous disc translate into the RC and the full 2D velocity field (VF) of galaxies. Distortions and declining RCs were found at distances larger than 12 kpc from the center of the galaxy, indicating the presence of an undisturbed inner part below that radius. The inclination of the galaxy relative to the line of sight changes the degree of disturbance and may shift the luminosity center from the kinematic one. In our sample the RCs cover radii up to ~ 10 kpc, and therefore we are not able to investigate possible distortions at larger radii. The absence of irregularities in the inner parts may be a hint towards this kind of effect. In addition, the compression of the gas in the central parts due to the pressure of the intracluster medium (ICM) can trigger new star formation and a subsequent brightening of the ram-pressure affected galaxy causing high-luminosity TF offsets. According to Kronberger et al. (2008a) RPS enhances the SFR by up to a factor of 3 over several hundred Myr. In total the mass of newly formed stars is about two times higher than in an isolated galaxy after 500 Myr of high ram pressure acting. However, these studies do not reach the ICM density conditions usually found in massive clusters. Ebeling et al. 2014 closed this gap and showed that cluster galaxies suffering strong ram pressure stripping (RPS) can increase their SF becoming temporarily brighter than even the BCG of the cluster. Although this is only expected to occur rarely and only in very massive clusters and for small angles between the normal vector of the disc and the vector of movement through the ICM, several such cases have been discovered (e.g. Owen et al. 2006, Cortese et al. 2007, Owers et al. 2012, Ebeling et al. 2014).

However, individual events of this intensity may be rare, requiring a gas-rich galaxy to cross deep within the cluster core at very high velocity. Steinhauser et al. (2016) went further in

this direction studying different infalling orbits for three distinct clusters finding that the star formation rate rises by up to 60% for galaxies with $V_{max}=170$ km/s in a cluster with similar properties of those we found in XMM2235-2557 after 0.5 Gyrs and following an orbit that goes through the very central regions of the cluster. We translate the SFR rise predicted by Kronberger et al. (2008a) and Steinhauser et al. (2016) into a change in B-band luminosity using the EzGal python code (Mancone & Gonzalez 2012). EzGal is a tool that takes models of how the SED of a stellar population evolves with time and projects it through filters to calculate several physical properties including magnitude evolution as a function of redshift. In our case we used the model libraries from Bruzual & Charlot 2003 to study the evolution of the B-band luminosity evolution after a short starburst caused by the compression of the gas in the inner disc due to RPS. We find a brightening of 0.9 and 0.3 magnitudes for Kronberger et al. (2008a) and Steinhauser et al. (2016) conditions respectively.

In summary, results from previous RPS studies and simulations point towards an enhancement of the SFR of the central regions of infalling cluster galaxies after going through the cluster environment for 500 Myrs, but maintaining undisturbed velocity fields in the inner parts as we find in our study. However, the variety of side effects playing a role in the process, such as inclination of the galaxy with respect to the infalling direction, density of the ICM, infalling velocity and gas fraction, makes it difficult to extract strong conclusions about the nature of the luminosity enhancement of our cluster galaxies without further observations.

In order to explore the connection between scaling relations for disc galaxies we compare in Fig. 4 the offsets ΔM_B from the TFR with the offsets $\Delta \log R_d$ from the VSR. By definition the median of both parameters is zero in the local universe. How-

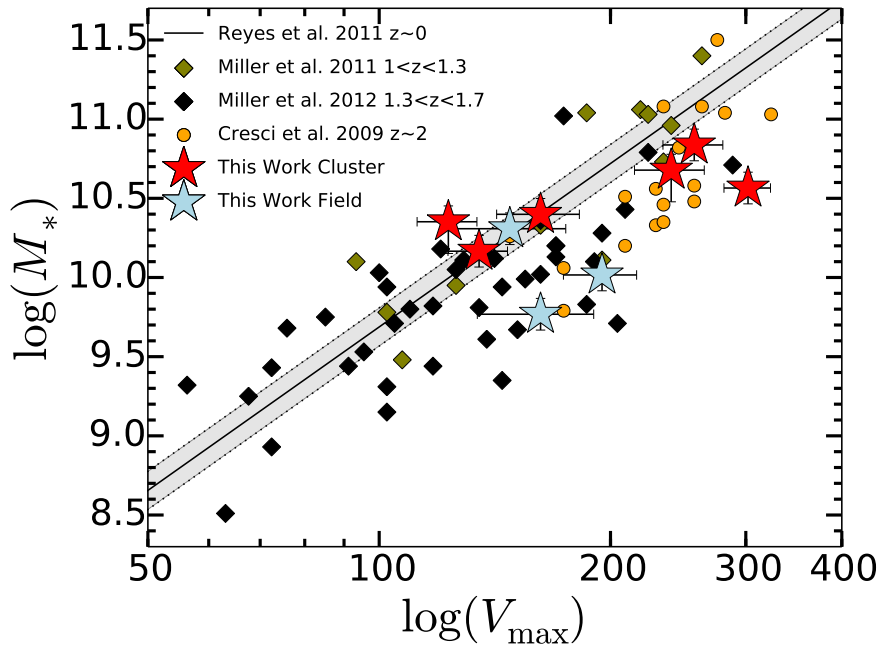


Fig. 5. Stellar mass Tully-Fisher relation. Red and blue stars are respectively cluster and field galaxies in our sample. Olive diamonds are 13 field galaxies at $1 < z < 1.3$ from Miller et al. (2011). Black diamonds show a sample of 42 field galaxies at $1.3 < z < 1.7$ from Miller et al. (2012) who found a well established M_* -TFR at this redshift. Orange circles are 18 field galaxies from Cresci et al. 2009 at $z \sim 2$. The solid line is the local M_* -TFR from Fig. 23 in Reyes et al. (2011), taking $V_{2.2}$ as V_{max} . The shaded area represents 1σ deviation from the previous relation.

ever there is a clear correlation between ΔM_B and $\Delta \log r_d$ given by the fact that luminosity, size and maximum velocity conform a three-dimensional parameter space in which disk galaxies populate a plane. Thus, these three parameters are correlated and deviations between local and distant galaxies reflect the evolution of one or several of the parameters. Fig. 4 shows the projection of this 3D-space on a luminosity-size plane represented by the offsets in disk scale length and absolute magnitude from the local VSR and TFR. This representation was recently used by BZ16 to study quantitatively the galaxy evolution in the field up to $z=1$. Using fixed-slope fits to determine the offsets from the local relation in terms of $\Delta \log R_d$, these authors found a combined evolution in size and luminosity in their sample with a zero point $\Delta \log R_d = -0.29$ for field galaxies at $0.59 < z < 1$, which is consistent with the slightly larger offset of our field sample (blue stars in figure 4) at slightly higher redshift $1 < z < 1.2$. However, cluster galaxies at $z=1.4$ show bigger offsets, and a zero point of $\Delta \log R_d = -0.59$. Although our cluster sample has large scatter, our data follow the general trend in the BZ16 sample at $0 < z < 1$: distant galaxies are shifting away from the local $\Delta M_B - \Delta \log R_d$ relation towards smaller sizes and higher luminosity with look-back time.

Assuming that galaxies in both samples are virialized, higher maximum velocity can only be explained by higher total mass values, including baryonic (stellar plus gas) and dark matter content. Since it is not possible to get direct information about the gas fraction for distant galaxies due to instrumental constraints, M_* is the only available quantity we have to explore the evolution of the baryonic mass in galaxies at this redshift. In Fig. 5 we investigate the stellar mass TFR (M_* -TFR) for the field and cluster galaxies in our sample. Our cluster sample is composed of two groups divided by their total mass (V_{max}): Three massive fast-rotating galaxies with $10.5 > \log M_* > 10.8$ embody the first group, while another three slow-rotating galaxies show slightly

lower stellar masses, $10.2 > \log M_* > 10.4$. Our results follow the M_* -TFR for spiral galaxies established by Miller et al. 2012 at redshift $1.3 < z < 1.7$ and are in agreement with previous studies at similar redshift like Miller et al. 2011 $z < 1.3$ and Cresci et al. 2009 at $z \sim 2$. We compare our dataset with the local M_* -TFR established by Reyes et al. 2011 using a subsample of local galaxies from SDSS DR7.

Combining the results from B-band TFR (Fig. 3A) and the M_* -TFR (Fig. 5), high total mass cluster galaxies show $\log M_* > 10.5$ and deviations around 2σ from the local TFR, while the low total mass galaxies display $\log M_* < 10.5$ and are shifted by more than 5 sigma towards higher B-band luminosities. One possible explanation for this behaviour would be that high mass distant galaxies have grown their stellar mass following star formation histories compatible with quiescent evolution excluding starbursting episodes in the last few billion years. In contrast, low mass galaxies at this epoch are still in the early phases of assembling their disk and are more prone to suffer environmental effects. The tendency for high mass galaxies to develop their disk first has been recently studied by Simons et al. (2016) for field galaxies up to $z \sim 2$ using MOSFIRE with three slit positions and obtaining similar results combining the TFR and M_* -TFR with a cut in stellar mass at $\log M_* = 10.2$.

It is known that distant galaxies are expected to be more luminous at high- z than their local counterparts for a given V_{max} , particularly in the B-band, which is sensitive to high-mass stars with short lifetimes. In addition, gas mass fractions are higher (Puech et al. 2010), corresponding to lower stellar to total mass ratios due to the fact that less gas has been converted into stars. Our sample of high mass cluster galaxies has a stellar-to-dynamical mass ratio smaller than the local value. This means that while the dynamical mass is already in place at this cosmic epoch, the stellar mass has yet to be formed. This has already

been observed for field galaxies at similar and higher redshift (Cresci et al. 2009, Gnerucci et al. 2011, Vergani et al. 2012).

5. Conclusions

Using the FORS2 instrument at the ESO Very Large Telescope, we have studied a sample of 25 galaxies in the XMMU2235-2557 field of view. We carried out a kinematic analysis for 6 cluster members at $z \sim 1.4$ and 3 field galaxies at $1 < z < 1.2$, determining their maximum rotation velocity V_{max} . Structural parameters (such as disk inclination, scale length, etc.) were derived on HST/ACS and HAWK-I images. We analyzed the distant Tully-Fisher and velocity-size relations in XMM2235-2557 and compare them with reference samples at similar redshift and the local universe taking into account additional results from galaxy evolution simulations. Our main findings can be summarized as follows:

1. At given V_{max} , cluster galaxies are more luminous (in rest-frame B-band) and smaller (in rest-frame z-band) than their local counterparts towards higher redshifts. By $z=1.4$ we find for cluster members an average brightening of $\langle \Delta M_B \rangle = -1.7$ mag in absolute B-band magnitude and a decrease in size by a factor of ~ 2 .
2. The cluster galaxies in XMM2235 are divided in two sub-samples according to their V_{max} , occupying two different loci in the TFR. The first one is composed by relatively slow rotating (low total mass) galaxies that appear offset from the local TFR by more than 5σ . The second lies within the 2σ deviation region, in agreement with previous observational findings (Böhm & Ziegler 2016) and semianalytic models for galaxies at similar redshift (Dutton et al. 2011). The galaxies in our sample show smaller offsets and scatter in the stellar mass TF diagram than in the B-band TF diagram. The sub-sample of fast rotating galaxies show $10.5 > \log M_* > 10.8$ while the others have slightly lower stellar masses, $10.2 > \log M_* > 10.4$. This might indicate that although both sub-samples have similar stellar mass, they are affected differently by cluster-specific processes, which strongly enhance the SFRs and, in turn, B-band luminosities in the low-mass sub-sample.
3. The origin of the TFR offsets for the group of slow rotating (low total mass) galaxies is not clear. We have discussed several possibilities to explain our results, such as the underestimation of V_{max} due to the shape of the RC, the presence of a magnitude bias in our sample, and a temporary brightening in the B-band luminosity of these galaxies caused by the interaction with the environment. A combination of the two latter options appears to be the most likely explanation for our findings. The effect of the Malmquist is limited and can not be the sole explanation for the offsets of the slow rotating subsample: $\langle \Delta M_B \rangle = -2.5$. Results from previous ram pressure stripping studies and simulations show that it is possible to enhance the SFR in the central regions of infalling cluster galaxies (and thus the B-band luminosity) maintaining undisturbed velocity fields (and RCs) at smaller radii than 3-4 scale lengths, as we find in our sample. However, the small size of our cluster sample together with the variety of effects playing a role in this process, such as inclination of the galaxy with respect to the infalling direction, density of the ICM, infalling velocity and gas fraction, and the combined possible effect of the magnitude bias make it difficult to draw firm conclusions about the nature of these offsets without further observations.
4. Analysis of the combined offsets in our sample from the Tully-Fisher and Velocity-Size relations reveal there is a correlation between them. Galaxies with a strong offset towards high B-band luminosity with respect to the local TFR have a similar size than their local counterparts at comparable V_{max} , while galaxies with offsets towards smaller sizes with respect to the local VSR have luminosities compatible with the local TFR. These results are in agreement with what was shown in a previous paper by Böhm & Ziegler 2016.

In this paper we have explored the kinematics of galaxies in a high redshift cluster. The distribution of our cluster sub-samples in the TFR suggest that there exist a population of galaxies that is consistent with the predicted evolutionary state of galaxies at this redshift, while cluster specific interactions such as RPS might be responsible of the B-band luminosity enhancement suffered by the other half. However, it is not clear how likely this kind of events are and whether the luminosity enhancement can be explained by a single process. Discriminating between the origin of TFR offsets of bright cluster galaxies will require further work, such as examining the difference in star formation rate for distant cluster galaxies and the use of larger data sets covering a wide range of environments within the cluster.

Acknowledgements. AB is grateful to the Austrian Science Fund (FWF) for funding (grant number P23946-N16).

References

- Angulo, R. E. & White, S. D. M. 2010, MNRAS, 405, 143
 Arnouts, S. & Ilbert, O. 2011, Astrophysics Source Code Library [ascl:1108.009]
 Bamford, S. P., Milvang-Jensen, B., Aragón-Salamanca, A., & Simard, L. 2005, MNRAS, 361, 109
 Bertin, E. 2009, Mem. Soc. Astron. Italiana, 80, 422
 Bertin, E. & Arnouts, S. 1996, A&AS, 117, 393
 Böhm, A., Wisotzki, L., Bell, E. F., et al. 2013, A&A, 549, A46
 Böhm, A. & Ziegler, B. L. 2007, ApJ, 668, 846
 Böhm, A. & Ziegler, B. L. 2016, A&A, 592, A64
 Böhm, A., Ziegler, B. L., Saglia, R. P., et al. 2004, A&A, 420, 97
 Bösch, B., Böhm, A., Wolf, C., et al. 2013, A&A, 554, A97
 Bouwens, R. J., Illingworth, G. D., Franx, M., & Ford, H. 2007, ApJ, 670, 928
 Bower, R. G., Benson, A. J., & Crain, R. A. 2012, MNRAS, 422, 2816
 Bruzual, G. & Charlot, S. 2003, MNRAS, 344, 1000
 Butcher, H. & Oemler, Jr., A. 1978, ApJ, 219, 18
 Chabrier, G. 2003, PASP, 115, 763
 Cortese, L., Marcillac, D., Richard, J., et al. 2007, MNRAS, 376, 157
 Courteau, S. 1997, AJ, 114, 2402
 Cresci, G., Hicks, E. K. S., Genzel, R., et al. 2009, ApJ, 697, 115
 de Jong, R. S. 1996, A&A, 313, 377
 Dekel, A., Birnboim, Y., Engel, G., et al. 2009, Nature, 457, 451
 Dutton, A. A., van den Bosch, F. C., Faber, S. M., et al. 2011, MNRAS, 410, 1660
 Ebeling, H., Stephenson, L. N., & Edge, A. C. 2014, ApJ, 781, L40
 Förster Schreiber, N. M., Genzel, R., Bouché, N., et al. 2009, ApJ, 706, 1364
 Genzel, R., Tacconi, L. J., Eisenhauer, F., et al. 2006, Nature, 442, 786
 Giovanelli, R., Haynes, M. P., Salzer, J. J., et al. 1995, AJ, 110, 1059
 Gnerucci, A., Marconi, A., Cresci, G., et al. 2011, A&A, 528, A88
 Grützbauch, R., Bauer, A. E., Jørgensen, I., & Varela, J. 2012, MNRAS, 423, 3652
 Hasinger, G., Miyaji, T., & Schmidt, M. 2005, A&A, 441, 417
 Haynes, M. P., Giovanelli, R., Chamaroux, P., et al. 1999a, AJ, 117, 2039
 Haynes, M. P., Giovanelli, R., Salzer, J. J., et al. 1999b, AJ, 117, 1668
 Heidmann, J., Heidmann, N., & de Vaucouleurs, G. 1972, MmRAS, 75, 85
 Ilbert, O., Arnouts, S., McCracken, H. J., et al. 2006, A&A, 457, 841
 Jaffé, Y. L., Aragón-Salamanca, A., Kuntschner, H., et al. 2011, MNRAS, 417, 1996
 Kapferer, W., Sluka, C., Schindler, S., Ferrari, C., & Ziegler, B. 2009, A&A, 499, 87
 Kelly, P. L., von der Linden, A., Applegate, D. E., et al. 2014, MNRAS, 439, 28
 Kelvin, L. S., Driver, S. P., Robotham, A. S. G., et al. 2012, MNRAS, 421, 1007
 Kron, R. G. 1980, ApJS, 43, 305

Table 2. General properties of our cluster and field samples. IDs, J2000 coordinates, redshift, AB absolute B-band magnitude, observed K-band magnitude, $J - K$ colours, logarithmic stellar mass.

ID	RA (hh:mm:ss)	DEC (dd:mm:ss)	z	M_B (mag)	m_K (mag)	$J - K$ (mag)	$\log M_*/M_\odot$
1	22:35:21.6	-25:54:30.4	1.364	-22.91	20.24	0.62	$10.98^{+0.07}_{-0.05}$
2	22:35:21.7	-25:54:39.4	1.391	-22.46	20.62	0.72	$10.67^{+0.07}_{-0.17}$
3	22:35:33.5	-25:55:08.7	1.366	-22.81	20.16	0.85	$10.57^{+0.09}_{-0.08}$
4	22:35:21.9	-25:55:38.9	1.391	-22.43	20.31	0.82	$10.99^{+0.10}_{-0.01}$
5	22:35:33.1	-25:55:47.1	1.358	-21.76	21.40	0.64	$10.17^{+0.08}_{-0.11}$
6	22:35:27.1	-25:56:34.7	1.386	-21.80	21.31	0.62	$10.49^{+0.05}_{-0.02}$
7	22:35:19.4	-25:56:56.0	1.380	-21.64	21.05	0.86	$10.74^{+0.05}_{-0.02}$
8	22:35:21.8	-25:57:14.0	1.399	-20.97	21.89	0.81	$10.35^{+0.08}_{-0.18}$
9	22:35:21.6	-25:57:38.6	1.389	-20.34	22.10	0.97	$10.32^{+0.15}_{-0.03}$
10	22:35:33.0	-25:57:57.4	1.390	-22.26	20.65	0.85	$10.58^{+0.07}_{-0.06}$
11	22:35:18.1	-25:58:06.6	1.382	-22.11	21.61	0.39	$10.40^{+0.07}_{-0.09}$
12	22:35:17.1	-25:58:35.4	1.395	-22.08	21.64	0.29	$10.10^{+0.08}_{-0.07}$
13	22:35:26.0	-25:58:53.5	1.388	-22.47	20.14	1.02	$11.05^{+0.04}_{-0.06}$
14	22:35:21.0	-25:59:03.8	1.395	-21.49	21.66	0.66	$10.11^{+0.08}_{-0.06}$
15	22:35:27.8	-25:59:48.8	1.353	-22.17	21.05	0.42	$10.68^{+0.09}_{-0.21}$
16	22:35:17.1	-26:00:26.3	1.357	-22.56	20.49	0.75	$10.84^{+0.09}_{-0.09}$
17	22:35:21.1	-26:01:22.8	1.397	-21.29	21.49	0.88	$10.40^{+0.17}_{-0.01}$
18	22:35:23.0	-25:54:58.8	0.560	-19.25	22.02	0.27	$9.26^{+0.06}_{-0.03}$
19	22:35:24.8	-25:55:27.0	0.994	-21.39	21.26	0.34	$10.02^{+0.09}_{-0.08}$
20	22:35:17.8	-25:56:05.2	0.765	-23.00	20.25	0.61	$10.69^{+0.04}_{-0.02}$
21	22:35:22.2	-25:56:20.0	1.511	-21.82	22.29	0.05	$9.91^{+0.05}_{-0.06}$
22	22:35:21.5	-25:57:30.2	1.091	-21.47	20.80	0.74	$10.39^{+0.08}_{-0.09}$
23	22:35:17.7	-25:59:14.3	0.884	-20.59	21.10	0.52	$10.03^{+0.06}_{-0.05}$
24	22:35:28.8	-26:00:10.3	0.986	-21.38	21.45	0.41	$9.70^{+0.09}_{-0.05}$
25	22:35:19.4	-26:01:08.1	1.167	-21.30	21.68	0.81	$9.83^{+0.09}_{-0.10}$

Table 3. Structural parameters of the cluster and field kinematic samples. IDs, redshifts, scale length (R_d), inclination (i), position angle (θ), misalignment (δ) and logarithmic stellar mass.

ID	z	R_d (kpc)	i ($^\circ$)	θ ($^\circ$)	δ ($^\circ$)	V_{max} (km/s)	$\log M_*/M_\odot$
3	1.366	3.4 ± 0.9	50	-29	2	305 ± 16	10.57
5	1.358	1.5 ± 0.9	70	-36	6	134 ± 12	10.17
8	1.399	4.1 ± 0.5	67	40	9	129 ± 12	10.35
11	1.382	3.9 ± 0.5	70	5	1	163 ± 20	10.40
15	1.353	4.8 ± 0.9	33	39	6	239 ± 20	10.68
16	1.357	1.6 ± 0.9	33	34	14	259 ± 13	10.84
19	0.994	3.4 ± 0.9	43	-45	15	195 ± 21	10.02
22	1.091	3.0 ± 0.9	39	75	30	149 ± 27	10.31
25	1.167	3.8 ± 0.9	42	-15	21	163 ± 28	9.77

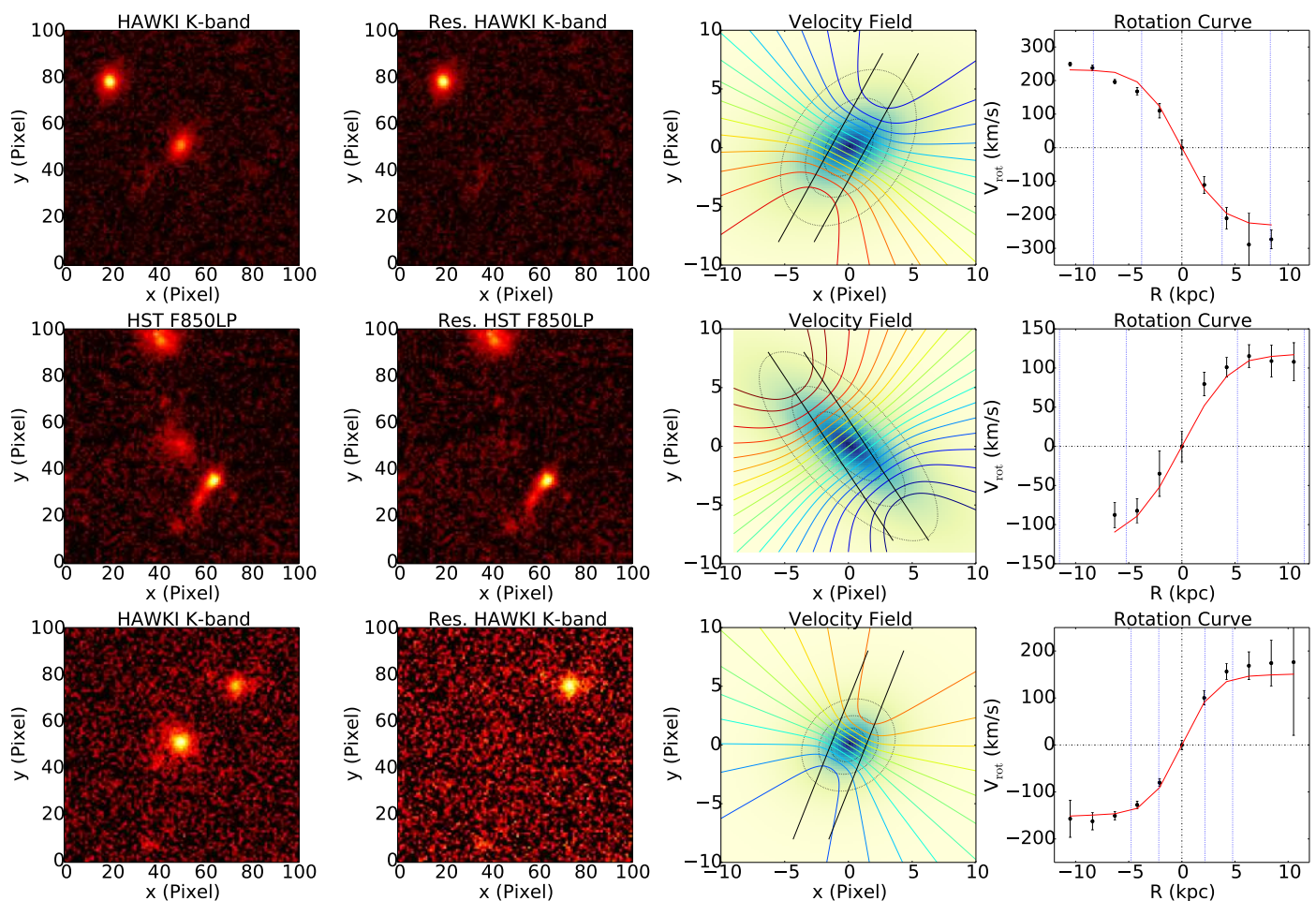


Fig. 6. Three examples of cluster galaxies analyzed following the methods explained in Sect. 3. The first column shows the HAWKI K-band image centered on the target galaxy. The second column displays the residuals after subtracting the 2D-model of the galaxy. The third column presents the synthetic velocity field based on the observed structural parameters after fitting the simulated rotation curve to the observed one. The black lines mark the position of the slit. The fourth column displays the rotation curve (black points) in the observed frame, and the fitted simulated RC (red line). The blue dashed lines mark the radii corresponding to 1 and 2.2 gas scale lengths.

- Kronberger, T., Kapferer, W., Ferrari, C., Unterguggenberger, S., & Schindler, S. 2008a, *A&A*, 481, 337
- Kronberger, T., Kapferer, W., Unterguggenberger, S., Schindler, S., & Ziegler, B. L. 2008b, *A&A*, 483, 783
- Kutdemir, E., Ziegler, B. L., Peletier, R. F., et al. 2010, *A&A*, 520, A109
- Kutdemir, E., Ziegler, B. L., Peletier, R. F., et al. 2008, *A&A*, 488, 117
- Lehnert, M. D., Nesvadba, N. P. H., Le Tiran, L., et al. 2009, *ApJ*, 699, 1660
- Lidman, C., Rosati, P., Tanaka, M., et al. 2008, *A&A*, 489, 981
- Lilly, S. J., Le Fevre, O., Hammer, F., & Crampton, D. 1996, *ApJ*, 460, L1
- Mancone, C. & Gonzalez, A. 2012, *EzGal: A Flexible Interface for Stellar Population Synthesis Models*, Astrophysics Source Code Library
- McGaugh, S. S., Schombert, J. M., Bothun, G. D., & de Blok, W. J. G. 2000, *ApJ*, 533, L99
- Miller, S., Ellis, R. S., Sullivan, M., Bundy, K., & Treu, T. 2012, in *American Astronomical Society Meeting Abstracts*, Vol. 219, American Astronomical Society Meeting Abstracts #219, 202.02
- Miller, S. H., Bundy, K., Sullivan, M., Ellis, R. S., & Treu, T. 2011, *ApJ*, 741, 115
- Milvang-Jensen, B., Aragón-Salamanca, A., Hau, G. K. T., Jørgensen, I., & Hjorth, J. 2003, *MNRAS*, 339, L1
- Mocz, P., Green, A., Malacari, M., & Glazebrook, K. 2012, *MNRAS*, 425, 296
- Moran, S. M., Miller, N., Treu, T., Ellis, R. S., & Smith, G. P. 2007, *ApJ*, 659, 1138
- Mullis, C. R., Rosati, P., Lamer, G., et al. 2005, *ApJ*, 623, L85
- Nakamura, O., Aragón-Salamanca, A., Milvang-Jensen, B., et al. 2006, *MNRAS*, 366, 144
- Owen, F. N., Keel, W. C., Wang, Q. D., Ledlow, M. J., & Morrison, G. E. 2006, *AJ*, 131, 1974
- Owers, M. S., Couch, W. J., Nulsen, P. E. J., & Randall, S. W. 2012, *ApJ*, 750, L23
- Peng, C. Y., Ho, L. C., Impey, C. D., & Rix, H.-W. 2002, *AJ*, 124, 266
- Peng, Y.-j., Lilly, S. J., Kovač, K., et al. 2010, *ApJ*, 721, 193
- Persic, M., Salucci, P., & Stel, F. 1996, *MNRAS*, 281, 27
- Pickles, A. J. 1998, *PASP*, 110, 863
- Pierce, M. J. & Tully, R. B. 1992, *ApJ*, 387, 47
- Puech, M., Flores, H., Hammer, F., et al. 2008, *A&A*, 484, 173
- Puech, M., Hammer, F., Flores, H., et al. 2010, *A&A*, 510, A68
- Reyes, R., Mandelbaum, R., Gunn, J. E., Pizagno, J., & Lackner, C. N. 2011, *MNRAS*, 417, 2347
- Rodrigues, M., Hammer, F., Flores, H., Puech, M., & Athanassoula, E. 2016, *ArXiv e-prints* [arXiv:1611.03499]
- Rosati, P., Tozzi, P., Gobat, R., et al. 2009, *A&A*, 508, 583
- Santos, J. S., Altieri, B., Popesso, P., et al. 2013, *MNRAS*, 433, 1287
- Schirmer, M. 2013, *ApJS*, 209, 21
- Simons, R. C., Kassim, S. A., Trump, J. R., et al. 2016, *ArXiv e-prints* [arXiv:1606.00009]
- Steinhauser, D., Schindler, S., & Springel, V. 2016, *A&A*, 591, A51
- Strazzullo, V., Rosati, P., Pannella, M., et al. 2010, *A&A*, 524, A17
- Tiley, A. L., Stott, J. P., Swinbank, A. M., et al. 2016, *ArXiv e-prints* [arXiv:1604.06103]
- Tonini, C., Maraston, C., Ziegler, B., et al. 2011, *MNRAS*, 415, 811
- Tully, R. B., Pierce, M. J., Huang, J.-S., et al. 1998, *AJ*, 115, 2264
- Vergani, D., Epinat, B., Contini, T., et al. 2012, *A&A*, 546, A118
- Wisnioski, E., Förster Schreiber, N. M., Wuyts, S., et al. 2015, *ApJ*, 799, 209
- Ziegler, B. L., Böhm, A., Jäger, K., Heidt, J., & Möllenhoff, C. 2003, *ApJ*, 598, L87